

Influence of extended defects on the formation energy, hyperfine structure, and zero-field splitting of NV centers in diamond

Wolfgang Körner ^{1,*}, Daniel F. Urban ¹ and Christian Elsässer^{1,2}

¹Fraunhofer Institute for Mechanics of Materials IWM, Wöhlerstraße 11, 79108 Freiburg, Germany

²University of Freiburg, Freiburg Materials Research Center (FMF), Stefan-Meier-Straße 21, 79104 Freiburg, Germany



(Received 17 September 2020; revised 3 December 2020; accepted 4 February 2021; published 15 February 2021)

We present a density-functional theory analysis of nitrogen-vacancy (NV) centers in diamond, which are located in the vicinity of extended defects, namely, intrinsic stacking faults, extrinsic stacking faults, and coherent twin boundaries on $\{111\}$ planes in diamond crystals. Several sites for NV centers close to the extended defects are energetically preferred with respect to the bulk crystal. This indicates that NV centers may be enriched at extended defects. We report the hyperfine structure and zero-field splitting parameters of the NV centers at the extended defects, which typically deviate by about 10% but in some cases up to 90% from their bulk values. Furthermore, we find that the influence of the extended defects on the NV centers is of short range: NV centers that are about three double layers (corresponding to ≈ 6 Å) away from defect planes already show bulklike behavior.

DOI: [10.1103/PhysRevB.103.085305](https://doi.org/10.1103/PhysRevB.103.085305)

I. INTRODUCTION

The negatively charged nitrogen vacancy (NV^-) in diamond consists of a substitutional nitrogen atom with a vacant nearest-neighbor carbon site and an additional electron. This point-defect complex has many promising applications, for example, as an almost-atomic probe for high spatial resolution magnetometry [1–3] or an optically addressable solid-state qubit for quantum computing [4].

Our motivation to study NV centers near extended defects like stacking faults (SFs) and grain boundaries (GBs) is twofold. In general, the properties of point defects are altered near such extended defects in a characteristic manner, which make the point defect a sensitive local probe for extended defects. In a recent study of Ivády *et al.* [5], the analysis of the electronic (hyperfine) structure enabled the assignment of previously unidentified divacancylike color centers in silicon carbide (SiC) which have an improved robustness against photoionization and show room-temperature stability. A second motivation is related to ensembles of NV centers acting together as sensitive magnetic probe arrays, for example, in the context of detection of microstructural defects in electronic devices or mechanical components. To achieve a high magnetic sensitivity, the ensemble of NV^- centers needs to be spatially localized and aligned, and the coherence time T_2 needs to be long enough (in the range of μs). Various groups of experimentalists could achieve highly aligned (up to 99%) ensembles of NV centers by means of chemical vapor deposition (CVD) [6,7]. Here, NV centers are localized within only a few-nanometer-thin layers. Thermal treatment of such layers can lead to conversion of further substitutional nitrogen atoms into NV^- centers and increase T_2 by annealing

lattice imperfections. However, thermal annealing may also reduce the alignment or even destroy NV centers under some conditions [6–8].

The CVD nucleation and growth processes for diamond create extended crystal defects, including twin boundaries, stacking faults, and dislocations, which are frequently oriented along $\{111\}$ planes [9]. Therefore, we consider a selection of such extended defects and their interplay with NV centers in this work. The presence of an extended defect may facilitate the alignment of the NV centers and also lead to an enrichment (segregation) of NV^- at the extended defect. For our study we selected the intrinsic SF (ISF; stacking sequence ABCABABC of $\{111\}$ layers), the extrinsic SF (ESF; stacking sequence ABCABACABC), and the coherent twin boundary (CTB; stacking sequence ABCACBA). We have built supercell models in which we have placed the NV centers at all possible sites relative to the planar defect and evaluated their total energies to clarify whether the sites are preferred with respect to the bulk crystal. Furthermore, we evaluated the hyperfine structure (HFS) and the zero-field splitting (ZFS) parameters. These provide the possibility to identify sites of different point defects since these quantities are accurately measurable with sensitive techniques such as optically detected magnetic resonance (ODMR) [4,10].

The paper is organized as follows: In Sec. II A the computational details and the supercell models are described. In Secs. II B–II D we briefly summarize important properties and the calculation of the tensors of hyperfine structure parameters A_{ij}^l and zero-field splitting parameters D_{ij} . The results of the total-energy calculations are presented in Sec. III A. The results for the ZFS and HFS calculations are reported and discussed in Secs. III B and III C, respectively. A summary in Sec. IV concludes the paper.

*wolfgang.koerner@iw.fraunhofer.de

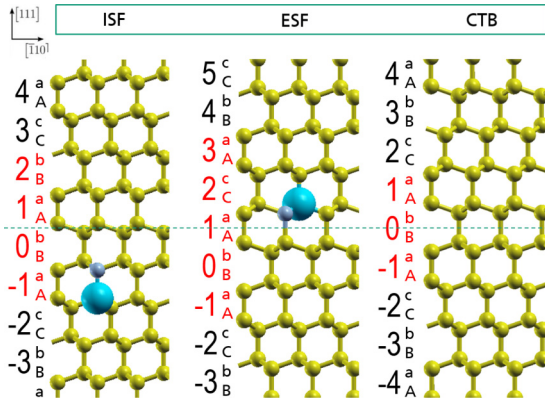


FIG. 1. Illustration of the atomic structure in the vicinity of the intrinsic stacking fault (ISF), the extrinsic stacking fault (ESF), and the coherent twin boundary (CTB). For later reference we assign numbers to all double layers. The yellow spheres represent the carbon atoms. In the left panel an axial NV center in layer $n = -1$ at position aA is shown and the middle panel includes a basal NV center in position aC. The position of the carbon vacancy is indicated by a large blue sphere and the nitrogen atom is represented by a small gray sphere. The horizontal dashed green line serves as a guide for the eye and indicates the center of the region where local hexagonal ordering is present, such as ABA or ACA. The respective double layers are highlighted with red labels. Note that the results displayed in the following figures will not be strictly symmetric with respect to this line because the NV defect complex has a defined orientation but no symmetry center between the N atom and the C vacancy.

II. THEORETICAL APPROACH

A. Supercell models

As a reference and starting system for the study of NV centers at $\{111\}$ extended defects we constructed a hexagonal supercell of the diamond single crystal consisting of $6 \times 6 \times 3$ hexagonal unit cells (six carbon atoms each) with the c axis pointing in $[111]$ direction. It thus contains $6^3 \times 3 = 648$ atoms. Cubic diamond (Ramsdell notation [11] 3C) in $[111]$ -direction shows a layered structure with the sequence unit ABC of periodic stacks of carbon layers. There also exists a hexagonal diamondlike polytype (Ramsdell notation [11] 2H) with the stacking sequence unit AB of carbon layers, which is named Lonsdaleite (see, e.g., Ref. [12] of Ownby *et al.* for the different polytypes of carbon). Lonsdaleite was taken as a second reference system because in the vicinity of extended defects the NV centers are sometimes located in a locally hexagonal atomic neighborhood. Our Lonsdaleite supercell consists of $6 \times 6 \times 5$ hexagonal unit cells (four carbon atoms each) with a total of 720 atoms in the supercell.

We have considered the three most prominent cases of extended planar $\{111\}$ defects, namely the ISF, ESF, and CTB. For the ISF we added two additional layers A and B to the bulk supercell (hence one C layer is missing). Since each double layer contains 72 atoms this supercell contains $648 + 144 = 792$ atoms in total. A close-up of the ISF region is shown in the left panel of Fig. 1. For the ESF, we inserted one additional layer A between a B and a C layer. This supercell contains $648 + 72 = 720$ atoms. The middle panel of Fig. 1 displays the atomic structure of the ESF region. To

obtain a CTB supercell, the layer sequence in the c direction is reversed in the upper half of the supercell. Here, our supercell contains 16 double layers yielding 1152 atoms in total. The CTB region is shown in the right panel of Fig. 1.

For the structural relaxation of the supercells mentioned above and the calculation of hyperfine structure parameters we used the Vienna ab initio simulation package (VASP) [13,14] version 5.4.4 with the projector-augmented-wave (PAW) method [15]. The exchange-correlation interactions are described by the generalized gradient approximation (GGA) of Perdew, Burke, and Ernzerhof (PBE) [16]. The VASP calculations were carried out with a plane-wave cutoff energy of 420 eV for the valence electrons.

For supercells with less than 800 atoms the Brillouin-zone integrals are evaluated on a Γ -centered $2 \times 2 \times 2$ k -point mesh with a Gaussian broadening of 0.05 eV. For larger supercells we considered only the Γ point. Atom positions were relaxed under constant volume until the residual forces acting on them were less than 0.01 eV/Å and the energy difference between two consecutive ionic relaxation steps was smaller than 10^{-5} eV.

We follow the work by Gali *et al.* [17] and use a lattice constant of $a = 3.567$ Å for the primitive cubic cell of diamond, which agrees well with the experimentally determined one of Holloway *et al.* [18]. Consequently, the length of the two lattice vectors in the basal plane of the hexagonal structure is 15.13 Å for all supercells. The c -axis lattice vectors vary in length from 18.53 Å (bulk diamond), to 20.59 Å (ESF and Lonsdaleite), 22.65 Å (ISF), and 32.95 Å (CTB).

In addition to the common ABC and AB notation of stacking sequences for close-packed cubic and hexagonal crystals, we also use the more detailed AaBbCc and AaBb notation for cubic and hexagonal diamond structures to specify precisely the positions of the NV centers. The left panel of Fig. 1 includes a NV center with the nitrogen atom at an a layer and the nearest-neighbor carbon vacancy at a layer A. NV centers that are oriented parallel to the $[111]$ direction are denoted *axial*. The NV center in the middle panel of Fig. 1 is inclined by about 109.5° with respect to the c axis and has the nitrogen atom in an a layer and the carbon vacancy in a C layer. NV centers in this orientation are denoted *basal*.

Note that the high C_{3v} symmetry of the NV^- is conserved for axially oriented NV centers near the extended defects. However, the presence of a NV center in basal orientation reduces the symmetry to C_{1h} , which implies a further splitting of levels, as discussed in the following.

To determine the interplay of the extended defects and the individual NV centers we have placed the NV^- defect at every symmetry-inequivalent axial and basal position within our supercells (with the N atom always in the layer a, b, or c and the carbon vacancy in the layer A, B, or C). For the discussion of results we assign numbers n to each double layer, cf. Fig. 1. The central region of the defects contain a number of double layers with a local hexagonal stacking. These are highlighted by red labels in the figure. For the ISF, the B layer $n = 0$ is sandwiched between two A layers with $n = \pm 1$. Also the A layer $n = 1$ has two neighboring layers of the same type, namely the B layers at $n = 0$ and $n = 2$. The ESF has two layers with local hexagonal stacking at positions $n = 0$ (ABA) and $n = 2$ (ACA). Finally, the CTB has only the layer $n = 0$ of

this type (here ABA). These special layer positions, where the regular ABC (or CBA) stacking of diamond in [111] direction is disturbed, will be important for the interpretation of our results, as presented in the following sections.

B. Hyperfine interaction

The hyperfine structure (HFS) tensor A^I describes the interaction between a nuclear spin S_I (located at site I) and the electronic spin distribution. The hyperfine interaction between a nuclear spin S_I (i.e., the nuclear spin of ^{13}C , ^{14}N , or ^{15}N) and the electronic spin distribution S_e (i.e., the spin of the defect state, $q = -1$, of the NV center) can be modeled with the Hamiltonian

$$H_{\text{HFS}} = S_e A^I S_I. \quad (1)$$

The hyperfine structure tensor components A_{ij}^I for a nucleus I are [19]

$$A_{ij}^I = \frac{\mu_0 \gamma_I \gamma_e}{2S} \int d^3 r n_S(\mathbf{r}) \left[\left(\frac{8\pi \delta(r)}{3} \right) + \left(\frac{3x_i x_j}{r^5} - \frac{\delta_{ij}}{r^3} \right) \right], \quad (2)$$

where the first term in brackets is the Fermi contact term and the second bracket is the magnetic dipole-dipole term. Here, $\mathbf{r} = [x_1, x_2, x_3]$ and n_S denotes the spin density associated with spin state S , μ_0 is the vacuum magnetic permeability, γ_e is the gyromagnetic ratio of the electron, and γ_I is the gyromagnetic ratio of the nucleus. In this work we use $\gamma(^{13}\text{C})/2\pi = 10.7084$ MHz/T, $\gamma(^{14}\text{N})/2\pi = 3.077$ MHz/T and $\gamma(^{15}\text{N})/2\pi = -4.316$ MHz/T, respectively [20].

The principal values A_{11} , A_{22} , and A_{33} of the hyperfine tensor which can be found by diagonalization are generally called hyperfine constants. If the hyperfine field has C_{3v} symmetry then $A_{11} = A_{22} =: A_{\perp}$ and $A_{33} =: A_{\parallel}$.

C. Zero-field splitting

The ZFS arises as consequence of various interactions of the electronic states of an atom or ion in a molecule or crystal due to the presence of more than one unpaired electron. The classic example for a ZFS is that of a spin triplet for a $S = 1$ spin system (as for the NV center in diamond). In the presence of an (externally applied) magnetic field, the degeneracy of the levels with different values of magnetic spin quantum number ($M_S = 0, +1, -1$) is lifted (magnetic Zeeman splitting). The effect of electron-electron repulsion by magnetic dipole-dipole interaction can be modeled by the Hamiltonian [21]

$$H_{\text{ZFS}} = \frac{\mu_0 g^2 \mu_B^2}{4\pi r^5} [3(\mathbf{S}_1 \cdot \mathbf{r})(\mathbf{S}_2 \cdot \mathbf{r}) - (\mathbf{S}_1 \cdot \mathbf{S}_2)r^2]. \quad (3)$$

Here, $r = |\mathbf{r}|$ with $\mathbf{r} = \mathbf{r}_1 - \mathbf{r}_2$ is the spatial distance between the spins, $\mathbf{S}_i = \frac{1}{2}[\sigma_x, \sigma_y, \sigma_z]$ is the spin operator vector of particle i , σ_j ($j = x, y, z$) are the Pauli matrices, and g is the Landé factor of free electrons. One can separate the spatial and spin dependencies in Eq. (3) and write the Hamiltonian in the form

$$H_{\text{ZFS}} = \mathbf{D} S, \quad (4)$$

where $S = S_1 + S_2$ is the total spin and \mathbf{D} describes the dipolar spin-spin interaction.

It can be shown that the tensor \mathbf{D} is symmetric and traceless and thus can be diagonalized. In the following, we name the diagonal elements D_{ii} . In general, one can split H_{ZFS} into a longitudinal component of the magnetic dipole-dipole interaction (named D) and a transversal component (named E). The Hamiltonian then reads

$$H_{\text{ZFS}} = D[S_z^2 - \frac{1}{3}S(S+1)] + E(S_x^2 - S_y^2), \quad (5)$$

with

$$D = \frac{3}{2}D_{zz} \text{ and } E = \frac{1}{2}(D_{xx} - D_{yy}). \quad (6)$$

The quantities D and E are accurately measurable with techniques such as ODMR [4,10] or electron paramagnetic resonance (EPR) [22,23].

An isolated NV center in a diamond crystal has C_{3v} symmetry. This axial symmetry implies $D_{xx} = D_{yy}$ and thus $E = 0$. When a NV center is close to an extended defect this degeneracy can be lifted significantly, as we discuss later. Of course, the same statement also holds for hyperfine structure constants and for axial symmetry $A_{xx} = A_{yy}$.

For more detailed information on the ZFS and HFS in diamond see, e.g., Refs. [21,23].

D. Computational details concerning A_{ij}^I and D_{ij}

The computation of the hyperfine structure tensor components A_{ij}^I and the zero-field-splitting tensor components D_{ij} was done with routines implemented in VASP. For the hyperfine structure tensor we follow the procedure of Szász *et al.* who carried out a careful analysis of the role of core spin polarization on the hyperfine structure constants [24]. They found that the underestimation of the localization of the wave function by the GGA functional PBE in general leads to incorrect results for the hyperfine structure constants A_{ij} , whereas using the hybrid functional HSE06 [25,26], which yields more localized wave functions, leads to results which differ only by a few percent from the experimental values. However, by neglecting the contribution of the core electrons (named A_{1c}) in the PBE calculations, one can obtain a quite good agreement with the experimental values as well. Due to the size of our supercell models (≈ 1000 atoms) we are restricted to the use of PBE and therefore apply the recipe of Szász *et al.* [24]. The quality of our results presented in Sec. III demonstrates that this approximation is apparently sufficient.

Well-relaxed structures are required as a prerequisite for calculating HFS constants as the HFS is sensitive to small structural changes. For the NV defect complex in the bulk diamond supercell, we compared the results for A_{ij} and D_{ij} for structures with forces relaxed to less than 0.01 and 0.001 eV/Å, respectively. The values of the diagonal elements D_{ii} of the ZFS tensor differed only by about 0.1% between the two cases. The values of the diagonal elements A_{ii} of the HFS tensor for ^{14}N differed by up to 1.2% and for ^{13}C by approximately 0.3%. The A_{ii} for ^{14}N have the largest variations since they have the smallest absolute values. For the smaller supercells we also performed convergence tests for the ZFS and HFS constants with respect to k -mesh and plane-wave cutoff parameters. We verified that a Γ -point calculation and a plane-wave cutoff energy of 420 eV is already sufficient

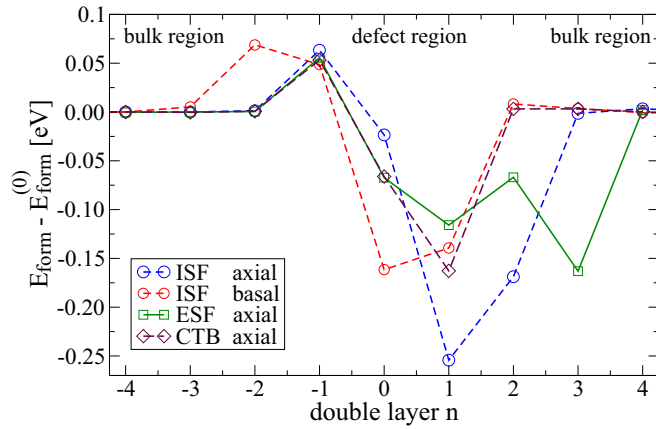


FIG. 2. Formation energies of NV centers with either axial or basal orientation in vicinity of an ISF, ESF, and CTB. Values are given in eV and are relative to the formation energy $E_{\text{form}}^{(0)}$ of NV centers in the bulklike region.

for numerically converged results for the supercells with the extended defects.

III. RESULTS AND DISCUSSION

All results reported in the following were obtained for negatively charged NV centers (NV^-).

A. Formation energies of nitrogen vacancy centers at extended defects

Figure 2 shows a selection of formation energies of NV centers with either axial or basal orientation at different positions relative to the considered extended planar defects. The values are given relative to the defect formation energy in the bulklike region, which we denote by $E_{\text{form}}^{(0)}$.¹ NV centers located at the double layers $n = 0, 1, 2$, or 3 have lower energies than in the bulk crystal and therefore are energetically favorable. The minimum value of approximately -0.25 eV is obtained for a NV^- in the axial position in double layer $n = 1$ at the ISF. For the double layers $n = -1$ and $n = -2$ most of the formation energies have slightly positive values. This asymmetry with respect to the center of the defect, as marked by the dashed green line in Fig. 1, originates in the orientation of the NV defect along the c axis.

An interesting question concerning extended defects is whether they can be used as structural templates for arranging an array of well-aligned and equally oriented NV centers. This

¹The NV-defect formation energy $E_{\text{form}}^{(0)}$ for the bulklike region was obtained from double layer $n = -4$. It agrees very well with the formation energy obtained from a bulk supercell calculation. The absolute values only differ by about 0.05 eV, which can be traced back to the different supercell sizes in the c direction. The fact that the obtained formation energies at double layers $n = \pm 4$ are very close to its bulk value $E_{\text{form}}^{(0)}$ is not due to the cancellation of the effects of two planar defects on the NV center in the supercell enforced by symmetry. The original symmetry of the supercell with an extended defect is always destroyed by the presence of the NV center.

would require a significant difference between the formation energies of the basal and axial orientation in addition to the condition that the formation energy of a NV center is lower at the extended defect than in the bulk crystal. For the ISF at the double layer $n = 1$ we found the largest difference in formation energies of approximately 0.1 eV. Since at room temperature 0.1 eV corresponds to a thermal energy of only $4k_B T$ we cannot expect a strict ordering of NV centers at ISF. For the ESF and the CTB the differences of the axial and basal orientations are even smaller. (We refrained from plotting these results for the basal orientation in the following figures for the sake of clarity).

B. Zero-field splitting

1. Longitudinal zero-field-splitting component D

For a NV^- center located in an otherwise perfect diamond crystal, the splitting of the singlet and triplet states of the 3A_2 ground state was experimentally determined to high precision by Felton *et al.* [22]: $D = \frac{3}{2}D_{zz} = 2.872(2)$ GHz. Our theoretical bulk value is $D_0 = 3.049$ GHz which deviates by 6.2% from the experimentally measured value. The deviation is partly coming from finite-size effects of our chosen bulk supercell ($6 \times 6 \times 3$). Test calculations with a bigger supercell consisting of $8 \times 8 \times 3$ hexagonal unit cells with 1151 atoms lead to a smaller deviation of only 4.0%.² Still we are far away from the situation encountered in experiments where the concentration of NV centers is in the range of a few ppm [7]. In our supercell models the NV density cannot significantly decrease below 1 : 1000 due to the computational limitations of DFT. Another source of error originates from the GGA approximation to the exchange-correlation functional of DFT, which affects the calculated charge densities. Finally, it has been shown that the approximation of the two-particle density by determinants of single-particle Kohn-Sham orbitals in the computation of the matrix elements of the ZFS-Hamiltonian [see Eq. (6) of Ref. [21]] is another source of error. This so-called spin contamination arises since these determinants are no exact eigenstates of the total-spin operator S (see Ref. [27] and references therein for more details).

In Fig. 3 the axial component D of the ZFS normalized to the bulk value D_0 is shown. At the ISF the axial oriented NV centers at the layers $n = 1$ and $n = 2$ have significantly reduced D values. At first glance these results are astonishing because one would expect this dip in D to be symmetric with respect to the center of the ISF. However, the main contribution to the ZFS originates from the three C atoms next to the vacancy, since they each have a magnetic moment of about $0.52\mu_B$ (in summary corresponding to 78% of $2\mu_B$). For the NV center located in the double layer $n = 1$ these carbon atoms are situated in layer b of the double layer $n = 0$ (cf. Fig. 1). Note that the double layers 0 and 1 of the ISF are locally in a hexagonal stacking ABA and BAB. The observed decrease of about 9% is consistent with the results $D_0 = 2.681$ GHz obtained for hexagonal Lonsdaleite (with

²Supercells for the ISF, ESF, and CTB with 8×8 hexagonal unit cells in the basal plane exceeded our computational resources.

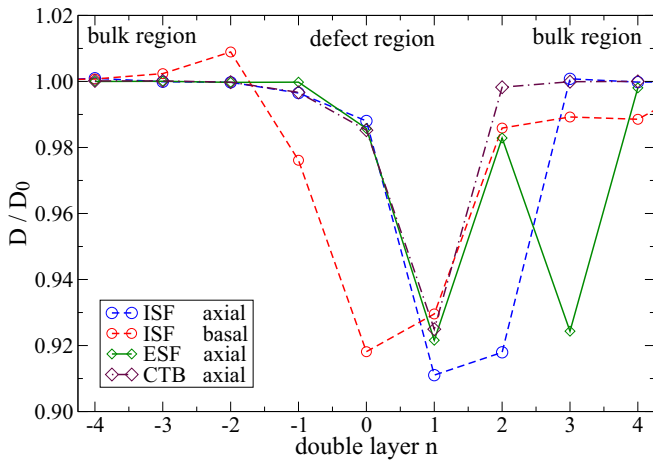


FIG. 3. Longitudinal component D of the ZFS of a NV^- center for different positions relative to the ISF, ESF, and CTB. Values are given with respect to the value D_0 of bulk diamond.

AB stacking). The latter value corresponds to about 88% of the value for diamond.

All the other dips observed in Fig. 3 can be explained in the same way by NV centers where the three carbon atoms next to the vacancy lie in a locally hexagonal layer-stacking sequence. At the ESF the two ABA stacking sequences are separated by one double layer, leading to a W shape of the data, while the curve for the CTB shows a V shape since there is only a single ABA stacking sequence.

2. Transversal zero-field-splitting component E

Figure 4 shows the calculated values of the transversal component E of the ZFS. The basal orientation of the NV center in combination with the extended defect breaks the threefold symmetry and thus E becomes nonzero. The influence of the extended defects on the transversal component E

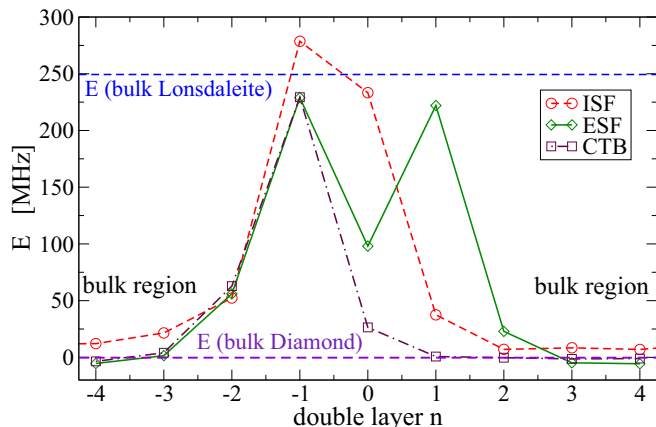


FIG. 4. Transversal component E of the ZFS (in MHz) for a NV center with basal orientation at different positions relative to the ISF, the ESF, and the CTB.

is apparently of short range and the E values quickly decay to zero with growing distance to the planar defect.³

Significant deviations in E from its bulk value occur whenever the three C atoms next to the C vacancy are located in an ABA-stacked neighborhood. For the ISF this is the case, e.g., for the NV center at the double layer $n = -1$, where E is about 278 MHz, and at $n = 0$, with 233 MHz which is close to the value obtained for the hexagonal Lonsdaleite, namely 249 MHz. It is conceivable that basally oriented NV centers at double layers $n = -1$ and $n = 0$ show approximately the transversal ZFS of Lonsdaleite. For the double layer $n = -1$, two carbon atoms are in the a layer of the double layer $n = -1$ and one carbon atom is in the b layer of double layer $n = 0$. This again results in a local hexagonally stacked neighborhood ABA (cf. Fig. 1). For the double layer $n = 0$, one carbon atom is in the a layer of double layer $n = 1$ while two carbon atoms are in the b layer of double layer $n = 0$, which yields the local hexagonally stacked neighborhood BAB.

The reasoning is similar for basal NV centers at the ESF and the CTB, which explains the (inverted) W and V shapes of the data sets. Like in the case of the longitudinal component D the magnitude of the extremal values for ESF and CTB are very similar and can be explained by the appearance of local hexagonal ABA or BAB stackings.

The finite E value leads to an additional splitting of the state 3A_2 (cf. Fig. 3 of Ref. [28]). For an external magnetic field B_{ext} in the [111] direction along the C_{3v} symmetry axis, the energy levels for a spin $S = 1$ system are [28]

$$E_{m_S=\pm 1} = D \pm \sqrt{E^2 + (g\mu_B B_{\text{ext}})^2}, \quad (7)$$

and $E_{m_S=0} = 0$, where m_S denotes the spin projection in the [111] direction.

C. Hyperfine structure

1. Hyperfine splitting connected to ${}^{14}\text{N}$ and ${}^{15}\text{N}$

Before discussing the results for the hyperfine structure constants at the three considered extended defects we compare our results for the NV center in the cubic diamond crystal to other theoretical and experimental results. In Table I the hyperfine structure parameters for ${}^{14}\text{N}$ and ${}^{15}\text{N}$ are given. In more recent experimental work [22], Felton *et al.* determined the sign of the parameters by measuring electron-nuclear double spin-flip transitions and apparently provide more accurate hyperfine parameters than He *et al.* [29] For more details we refer the reader to the discussion given in Ref. [22].

For all hyperfine structure constants the different theoretical studies agree with the experimental work of

³The value zero is not exactly obtained due to the finite size of the supercells with periodic boundary conditions. A basal NV center in our $6 \times 6 \times 3$ hexagonal supercell of the diamond bulk crystal has a finite value of $E_0 = 25$ MHz. Ideally E_0 should be zero in this case. However, the value zero is only numerically obtained for axially oriented NV centers in a hexagonal supercell for which the c axis is aligned with the NV center and the full symmetry is conserved. The values given in Fig. 4 are corrected by this offset E_0 (which also explains the slightly negative E values for the ESF and the CTB in the figure).

TABLE I. Comparison of hyperfine structure parameters A_{\parallel} and A_{\perp} for ^{14}N and ^{15}N in bulk diamond for the 3A_2 ground state. Our absolute values differ from the experimental values of Felton *et al.* [22] but the ratios A_{\parallel}/A_{\perp} agree quite well.

Defect in bulk diamond	A_{\parallel} [MHz]	A_{\perp} [MHz]	A_{\perp}/A_{\parallel}
$^{14}\text{NV}^-$ (this work, PBE)	-1.73	-2.16	1.25
$^{14}\text{NV}^-$ (expt.) ^a	-2.14(7)	-2.70(7)	1.26
$^{14}\text{NV}^-$ (expt.) ^b	+2.30(2)	-2.10(10)	1.10
$^{14}\text{NV}^-$ (theor., LSDA) ^c	-1.7	-1.7	1.00
$^{14}\text{NV}^-$ (theor., PBE) ^d	-1.71	-2.12	1.24
$^{14}\text{NV}^-$ (theor., HS06) ^d	-2.38	-2.79	1.17
$^{15}\text{NV}^-$ (this work, PBE)	2.43	3.03	1.25
$^{15}\text{NV}^-$ (expt.) ^a	3.03(3)	3.65(3)	1.21
$^{15}\text{NV}^-$ (theor., PBE) ^e	2.3	2.7	1.17

^aRef. [22].

^bRef. [29].

^cRef. [19].

^dRef. [24].

^eRef. [30].

Felton *et al.* [22] regarding the signs but not in the absolute values for which there are some considerable deviations. Gali *et al.* [19] report an isotropic hyperfine interaction for ^{14}N since their $b = (A_{\parallel} - A_{\perp})/3$ is zero. By contrast, our value is $b \approx 0.14$ MHz, which is in the range of 0.19(7) MHz measured by Felton *et al.* For ^{15}N , both Gali *et al.* [19] and we find an anisotropic interaction. Reference [19] reports $b \approx -0.13$ MHz, while our value is $b \approx -0.20$ MHz, which again is very close to the measured value $-0.21(3)$ MHz of Ref. [22].

The work of Szász *et al.* [24] basically agrees with our absolute values and the little deviations stem from the use of different supercell models. Our results are obtained from the 648-atom hexagonal supercell whereas they have used a 512-atom simple cubic supercell.

The theoretical results obtained with the HSE06 functional on the 512-atom supercell show the least deviations from the absolute experimental values of Felton *et al.* but the ratio A_{\perp}/A_{\parallel} deviates. Our calculated ratios A_{\perp}/A_{\parallel} for ^{14}N and ^{15}N agree reasonably well with the experimental data.

Figure 5 shows the results for the hyperfine structure constants for the ISF. For axially oriented NV centers all three diagonal elements A_{ii} ($i = 1, 2, 3$) increase by about 10% at layer $n = 0$ whereas they decrease by about 10% at layer $n = 2$. However, the ratio A_{\perp}/A_{\parallel} remains almost constant. The situation is rather different for the basal orientation of the NV center. Here, we observe a huge decrease of about +1.5 MHz for all three A_{ii} . For A_{33} this corresponds to a reduction of 90% in close vicinity to the defect plane. The diagonal elements A_{11} and A_{22} decrease by about 70% at layer $n = 1$ and show a small splitting of 0.02 to 0.06 MHz due to the presence of the ISF.

Of course, in the case of the nitrogen hyperfine interaction the location of the N atom (and not the location of the C atoms) is decisive. The strongest decrease of the hyperfine parameters occurs when the N atom is located in the double layer $n = 0$ or $n = 1$ where it is embedded in an ABA-stacked neighborhood.

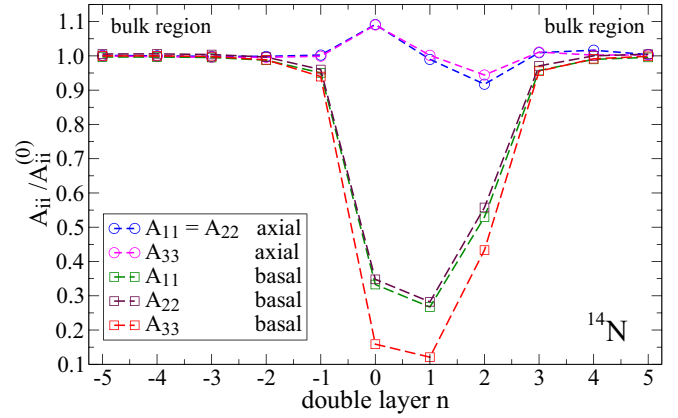


FIG. 5. Hyperfine structure constants A_{ii} for ^{14}N for the different positions at the ISF with either axial or basal orientation of the NV center. The A_{ii} values are normalized by the corresponding values $A_{ii}^{(0)}$ of bulk diamond.

The A_{ii} values for the ESF and CTB (not included in the figure) show the same magnitude of absolute variation as obtained for the ISF. The data show the characteristic W shape for the ESF and the V shape for the CTB, as previously observed for the D and E components of the ZFS (cf. Figs. 3 and 4, respectively).

2. Hyperfine splitting connected to ^{13}C

A compilation of hyperfine structure parameters for ^{13}C for bulk cubic diamond is listed in Table II, including our results and values taken from literature. The comparison of the most recent theoretical PBE results of Gali *et al.* [30], Szász *et al.* [24], and ourselves to the most recent experimental results of Felton *et al.* [22] yields a satisfactory agreement. Interestingly the theoretical results obtained with the more sophisticated HSE06 functional deviate more from the experimental results than those obtained by using the PBE functional. We therefore conclude that the latter provides an excellent starting point

TABLE II. Comparison of hyperfine structure parameters for ^{13}C in the cubic diamond crystal, where the ^{13}C is located at one of the three carbon sites next to the vacancy. Our calculated hyperfine structure constants agree very well with those determined experimentally in Ref. [22].

Bulk $^{14}\text{NV}^-$ center	A_{\parallel} [MHz]	A_{\perp} [MHz]	A_{\parallel}/A_{\perp}
^{13}C (this work, PBE)	199.9	119.2	1.68
^{13}C (expt.) ^a	199.7(2)	120.3(2)	1.66
^{13}C (expt.) ^b	± 205	± 123	1.67
^{13}C (theor., LSDA) ^c	185.4	109.9	1.69
^{13}C (theor., PBE) ^d	201.1	120.1	1.67
^{13}C (theor., PBE) ^e	199.8	119.8	1.67
^{13}C (theor., HSE06) ^e	228.8	144.5	1.58

^aRef. [22].

^bRef. [23].

^cRef. [19].

^dRef. [30].

^eRef. [24].

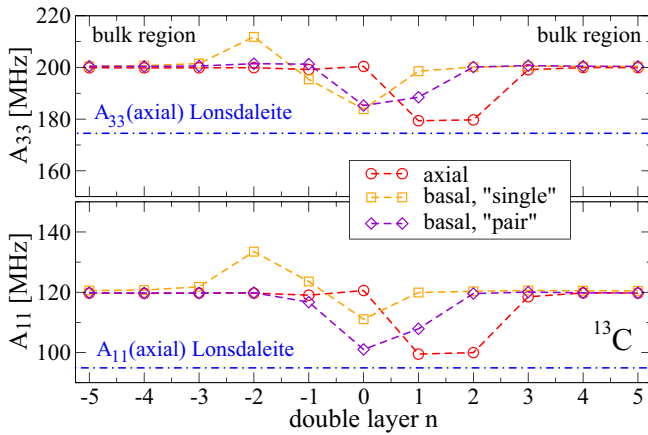


FIG. 6. Hyperfine structure constants A_{11} (lower panel) and A_{33} (upper panel) for ^{13}C for the various positions relative to the ISF with either axial or basal orientation of the NV center. For the basally oriented NV centers two carbon atoms lie in a common layer. Their values are denoted “pair.” The third carbon atom residing in the layer above the vacancy is denoted “single.”

for studying the effects of the extended defects on the hyperfine splitting. Note that in the early work of Loubser *et al.* [23] electron paramagnetic resonance was used which does not allow us to determine the sign of the hyperfine structure constants.

As in the case of nitrogen we present the hyperfine interaction results only for the ISF in Fig. 6 since these are sufficiently representative. For the axially oriented NV^- center the strongest decrease of the A_{ii} is of about 20 MHz at double layers $n = 1$ and $n = 2$. Again, like in the case of the ZFS, the minimum is shifted by one double layer to the right relative to the center of the ISF. This is conceivable since we look at the hyperfine interaction of ^{13}C atoms located at one of the three sites next to the C vacancy. Thus for an axial NV center situated at double layer $n = 1$ the respective ^{13}C atom is situated in layer b of double layer $n = 0$ and locally in a hexagonal ABA neighborhood. The reduced A_{ii} values are consistent with those obtained for Lonsdaleite (see blue dashed-dotted lines in Fig. 6).

The behavior of the NV center with the basal orientation is more complex. Like for ^{14}N , some A_{ii} values increase and others decrease. However, the ^{13}C atom can be located in two different layers. There are two sites for carbon atoms in the same layer of the nitrogen atom, which we call “pair,” and one site in the layer above the vacancy, which we denote “single.” The presence of an extended defect changes the charge distribution. Wherever the A_{ii} values are lowered the underlying reason is a reduced charge density [see Eq. (2)]. When A_{ii} is higher than in the bulk we found an increased charge density at the respective ^{13}C atom.

Furthermore, we obtained a splitting of A_{11} and A_{22} by 0.1 to 0.2 MHz at the pair sites and by 0.2 to 0.6 MHz at the single sites. This splitting originates in the breaking of the C_{3v} symmetry for the basally oriented NV centers induced by the presence of the extended defects. A similar splitting is observed when modeling the NV center in bulk diamond in a cubic supercell, which also breaks the C_{3v} symmetry (see

Supplemental Material of Ref. [24]). Note the much smaller order of magnitude of this induced splitting compared with the absolute values of the A_{ii} . We did not include the A_{22} components in Fig. 6 for the sake of clarity.

IV. SUMMARY

We have studied the influence of extended planar defects on the formation energies, zero-field splittings and hyperfine structures of negatively charged NV centers in diamond crystals. Our study includes the most relevant planar defects in {111} orientation in diamond, namely, intrinsic stacking faults, extrinsic stacking faults, and coherent twin boundaries. Altogether, there is a tendency of NV^- centers to be located at ISF, ESF, or CTB, since their formation energy is reduced compared with the bulk crystal for several sites in vicinity of the defect plane. However, for all the considered extended defects the energy differences between axially and basally oriented NV^- centers are small (0.1 eV or less) so that a preferential alignment of them may not necessarily be expected.

The hyperfine structure constants as well as the zero-field splitting parameters are influenced by the extended defects only in a very short range of a few atomic double layers.

The axial component D of the ZFS of a NV^- center, responsible for the singlet-triplet splitting, is at most reduced by about 9% in the environment of an extended defect. For basally oriented NV centers the transversal component E of the ZFS is not zero. Depending on the site and the extended defect type we obtain E values of about 250 ± 30 MHz, which cause a splitting of the triplet levels. The key structural elements causing the changes and the splittings are local hexagonal ABA-stacking sequences, like in hexagonal Lonsdaleite, which disturb the ABC-stacking sequence of cubic diamond.

For axially oriented NV^- centers the HFS constants A_{ii} for ^{14}N increase or decrease by approximately 10% and for basal orientation the A_{ii} almost vanish at local hexagonally stacked layers. The HFS constants A_{ii} for ^{13}C decrease by about 20 MHz for axially oriented NV^- centers near the extended defects and for basal orientation the A_{ii} decrease or increase (ranging from 101 to 131 MHz for A_{11} and A_{22} and from 185 to 212 MHz for A_{33}) depending on the reduction or accumulation of charge at the site of the carbon probe atom. All of the changes of the hyperfine constants are related to the appearance of the key structural element, namely, local hexagonal ABA stacks.

In conclusion, we believe that our results for the ZFS and the HFS help to interpret spectra of NV doped diamond samples. On the one hand, variations in the measured spectra of individual NV centers may be traced back to the presence of extended defects. On the other hand, for sufficiently high densities of NV centers, the spectral ODMR [6,7] data may allow us to obtain information about the distribution of extended defects with the NV centers acting as probes in the sample. The modified levels of NV centers close to extended defects should modify the shape of the tail of the dominant dip in frequency observed in ODMR measurements. However, mechanical strain and the presence of additional point defects like nearby vacancies or substitutional nitrogen atoms can influence the ZFS and HFS as well [21].

ACKNOWLEDGMENT

Financial support for this work was provided by the Fraunhofer Lighthouse Project Quantum Magnetometry (QMag).

-
- [1] G. Balasubramanian, I. Y. Chan, R. Kolesov, M. Al-Hmoud, J. Tisler, C. Shin, C. Kim, A. Wojcik, P. R. Hemmer, A. Krueger, T. Hanke, A. Leitenstorfer, R. Bratschitsch, F. Jelezko, and J. Wrachtrup, *Nature (London)* **455**, 648 (2008).
- [2] J. R. Maze, P. L. Stanwix, J. S. Hodges, S. Hong, J. M. Taylor, P. Cappellaro, L. Jiang, M. V. G. Dutt, E. Togan, A. S. Zibrov, A. Yacoby, R. L. Walsworth, and M. D. Lukin, *Nature (London)* **455**, 644 (2008).
- [3] V. M. Acosta, E. Bauch, M. P. Ledbetter, C. Santori, K. M. C. Fu, P. E. Barclay, R. G. Beausoleil, H. Linget, J. F. Roch, F. Treussart, S. Chemerisov, W. Gawlik, and D. Budker, *Phys. Rev. B* **80**, 115202 (2009).
- [4] V. Jacques, P. Neumann, J. Beck, M. Markham, D. Twitchen, J. Meijer, F. Kaiser, G. Balasubramanian, F. Jelezko, and J. Wrachtrup, *Phys. Rev. Lett.* **102**, 057403 (2009).
- [5] V. Ivády, J. Davidsson, N. Deegan *et al.*, *Nat. Commun.* **10**, 5607 (2019).
- [6] H. Ishiwata, M. Nakajima, K. Tahara, H. Ozawa, T. Iwasaki, and M. Hatano, *Appl. Phys. Lett.* **111**, 043103 (2017).
- [7] C. Osterkamp, M. Mangold, J. Lang *et al.*, *Sci. Rep.* **9**, 5786 (2019).
- [8] H. Ozawa, H. Ishiwata, M. Hatano, and T. Iwasaki, *Phys. Status Solidi A* **215**, 1800342 (2018).
- [9] S. Kaboli and P. C. Burnley, *Mater. Charact.* **142**, 154 (2018).
- [10] V. M. Acosta, E. Bauch, M. P. Ledbetter, A. Waxman, L.-S. Bouchard, and D. Budker, *Phys. Rev. Lett.* **104**, 070801 (2010).
- [11] L. S. Ramsdell, *Am. Mineral.: J. Earth Planetary Mater.* **32**, 64 (1947).
- [12] P. D. Ownby, X. Yang, and J. Liu, *J. Am. Ceram. Soc.* **75**, 1876 (1992).
- [13] G. Kresse and J. Furthmüller, *Phys. Rev. B* **54**, 11169 (1996).
- [14] G. Kresse and D. Joubert, *Phys. Rev. B* **59**, 1758 (1999).
- [15] P. E. Blöchl, *Phys. Rev. B* **50**, 17953 (1994).
- [16] J. P. Perdew, K. Burke, and M. Ernzerhof, *Phys. Rev. Lett.* **77**, 3865 (1996).
- [17] A. Gali, E. Janzeń, P. Deák, G. Kresse, and E. Kaxiras, *Phys. Rev. Lett.* **103**, 186404 (2009).
- [18] H. Holloway, K. C. Hass, M. A. Tamor, T. R. Anthony, and W. F. Banholzer, *Phys. Rev. B* **44**, 7123 (1991).
- [19] A. Gali, M. Fyta, and E. Kaxiras, *Phys. Rev. B* **77**, 155206 (2008).
- [20] M. A. Bernstein, K. F. King, and X. J. Zhou, *Handbook of MRI Pulse Sequences* (Elsevier Academic Press, San Diego, 2004), p. 960.
- [21] V. Ivády, T. Simon, J. R. Maze, I. A. Abrikosov, and A. Gali, *Phys. Rev. B* **90**, 235205 (2014).
- [22] S. Felton, A. M. Edmonds, M. E. Newton, P. M. Martineau, D. Fisher, D. J. Twitchen, and J. M. Baker, *Phys. Rev. B* **79**, 075203 (2009).
- [23] J. H. N. Loubser and J. A. van Wyk, *Rep. Prog. Phys.* **41**, 1201 (1978).
- [24] K. Szász, T. Hornos, M. Marsman, and A. Gali, *Phys. Rev. B* **88**, 075202 (2013).
- [25] J. Heyd, G. E. Scuseria, and M. Ernzerhof, *J. Chem. Phys.* **118**, 8207 (2003).
- [26] A. V. Krukau, O. A. Vydrov, A. F. Izmaylov, and G. E. Scuseria, *J. Chem. Phys.* **125**, 224106 (2006).
- [27] T. Biktagirov, W. G. Schmidt, and U. Gerstmann, *Phys. Rev. Res.* **2**, 022024(R) (2020).
- [28] R. Boča, *Coord. Chem. Rev.* **248**, 757 (2004).
- [29] X.-F. He, N. B. Manson, and P. T. H. Fisk, *Phys. Rev. B* **47**, 8816 (1993).
- [30] A. Gali, *Phys. Rev. B* **80**, 241204(R) (2009).